Compressive dynamic scission of carbon nanotubes under sonication: fracture by atomic ejection

H. B. Chew, M.-W. Moon, K. R. Lee and K.-S. Kim

Supplementary data	"Data Supplement" http://rspa.royalsocietypublishing.org/content/suppl/2010/12/07/rspa.2010.0495.DC1.html "Data Supplement" http://rspa.royalsocietypublishing.org/content/suppl/2010/12/07/rspa.2010.0495.DC2.html "Data Supplement" http://rspa.royalsocietypublishing.org/content/suppl/2010/12/07/rspa.2010.0495.DC3.html
References	**This article cites 32 articles, 3 of which can be accessed free** http://rspa.royalsocietypublishing.org/content/467/2129/1270.full.html#ref-list-1
Subject collections	Articles on similar topics can be found in the following collections materials science (217 articles) mechanical engineering (187 articles) nanotechnology (169 articles)
Email alerting service	Receive free email alerts when new articles cite this article - sign up in the box at the top right-hand corner of the article or click **here**

To subscribe to *Proc. R. Soc. A* go to: **http://rspa.royalsocietypublishing.org/subscriptions**

Compressive dynamic scission of carbon nanotubes under sonication: fracture by atomic ejection

By H. B. Chew[1], M.-W. Moon[2], K.-R. Lee[2] and K.-S. Kim[1],*

[1]*School of Engineering, Brown University, Providence, RI 02912, USA*
[2]*Computational Science Center, Interdisciplinary Fusion Technology Division, Korea Institute of Science and Technology, Seoul 136-791, Korea*

We report that a graphene sheet has an unusual mode of atomic-scale fracture owing to its structural peculiarity, i.e. single sheet of atoms. Unlike conventional bond-breaking tensile fracture, a graphene sheet can be cut by in-plane compression, which is able to eject a row of atoms out-of-plane. Our scale-bridging molecular dynamics simulations and experiments reveal that this compressive atomic-sheet fracture is the critical precursor mechanism of cutting single-walled carbon nanotubes (SWCNTs) by sonication. The atomic-sheet fracture typically occurs within 200 fs during the dynamic axial buckling of a SWCNT; the nanotube is loaded by local nanoscale flow drag of water molecules caused by the collapse of a microbubble during sonication. This is on the contrary to common speculations that the nanotubes would be cut in tension, or by high-temperature chemical reactions in ultrasonication processes. The compressive fracture mechanism clarifies previously unexplainable diameter-dependent cutting of the SWCNTs under sonication.

Keywords: atomic scission; carbon nanotube; buckling; nanofluidics; sonication

1. Introduction

Since the discovery of carbon nanotubes by Iijima (1991), cutting carbon nanotubes into shorter pieces has been crucial in scientific research and for technological applications that require highly specific nanotube lengths. The most widely adopted method of cutting was introduced by Liu *et al.* (1998) more than a decade ago and involves ultrasonication of single-walled carbon nanotubes (SWCNTs) in an aqueous medium. It was also discovered that the cutting rate under ultrasonication depends on the diameter of the carbon nanotube, and the dependence has been used for diameter sorting of the

*Author for correspondence (kyung-suk_kim@brown.edu).

Electronic supplementary material is available at http://dx.doi.org/10.1098/rspa.2010.0495 or via http://rspa.royalsocietypublishing.org.

nanotubes (Heller *et al.* 2004; Hennrich *et al.* 2007; Casey *et al.* 2008). Though the mechanism of cutting has been widely attributed to the collapse of cavitated microbubbles during sonication (Liu *et al.* 1998; Heller *et al.* 2004; Hennrich *et al.* 2007), the nanoscale cutting mechanism of SWCNTs under ultrasonication and the associated diameter-dependent cutting rate are still not well understood.

Regarding the microbubble dynamics, the Rayleigh–Plesset equation well describes the growth and the collapse of a single-cavitated bubble in an aqueous medium under sinusoidal pressure variations (Rayleigh 1917; Plesset & Prosperetti 1977). Both the Rayleigh–Plesset equation and experiments show that the microbubble grows slowly during the negative pressure phase of the sinusoidal loading, but collapses during the positive loading phase with four orders of magnitude greater speeds, which approach the sound wave speed in the liquid (Matula 1999; Brenner *et al.* 2002*a*). As such, extraordinary levels of energy focusing are achieved during the collapse period. In the vapour side, i.e. inside the bubble, the bubble collapse leads to adiabatic compression of the gases, which causes sonoluminescence (McNamara *et al.* 1999; Flannigan & Suslick 2005; Suslick & Flannigan 2008). In the liquid side, i.e. outside the bubble, the aqueous medium near the surface experiences exceptionally high-strain rate deformation (Brenner *et al.* 2002*a*). The former suggests the possibility of the nanotubes being sonochemically cut under ultrasonication, while the latter suggests mechanical loading.

Some have speculated that the collapse of microbubbles during sonication 'produces microscopic domains of high temperature leading to localized sonochemistry that attacks the surface of the nanotubes' (Liu *et al.* 1998; p. 1254); others have hypothesized that SWCNTs would be cut under axial tension if the nanotube is by chance aligned normal to the bubble wall (Hennrich *et al.* 2007). In investigating this mechanism, we have discovered that the SWCNT is, surprisingly, cut under axial compression by a unique mode of atomic-sheet fracture, in which the crack grows dynamically by the ejection of atoms. This compressive atomic-sheet fracture is brittle in contrast to defect-mediated bond breaking in the SWCNT under tension which would result in substantial ductile plastic elongation of the tube (Bosovic *et al.* 2003). Such a mechanism of compressive crack growth is unique to single atomic-sheet structures and has never been observed before.

When a SWCNT-dispersed aqueous medium is sonicated by a sonicator with a driving frequency of 20 kHz as shown in figure 1*a*, multiple bubbles of many different sizes are generated, with the larger bubbles distributed near the sonicator. The effective density gradient created by the bubble distribution then drives the convective current and establishes an optimal zone where the nanotubes are effectively cut. Solution of the Rayleigh–Plesset equation in figure 1*b* (Brenner *et al.* 2002*a*) shows that the optimal spherical bubble typically grows to a maximum size of approximately 30 μm radius, and collapses rapidly within approximately 4 μs during the compression cycle of sonication. If the maximum radius is considerably larger than approximately 30 μm, the bubble loses its spherical symmetry during the collapse cycle, thus reducing the effective strain rate of bubble shrinkage. If the bubble size is too small, the strain rate becomes too low to cut the SWCNT. During the expansion stage of the bubble growth with the expansion speed v_r of the radius R, the expansion strain rate ($\dot{\varepsilon} = v_r/R$) of the bubble wall is relatively low at less than $2 \times 10^5 \, \text{s}^{-1}$, and the SWCNT resides
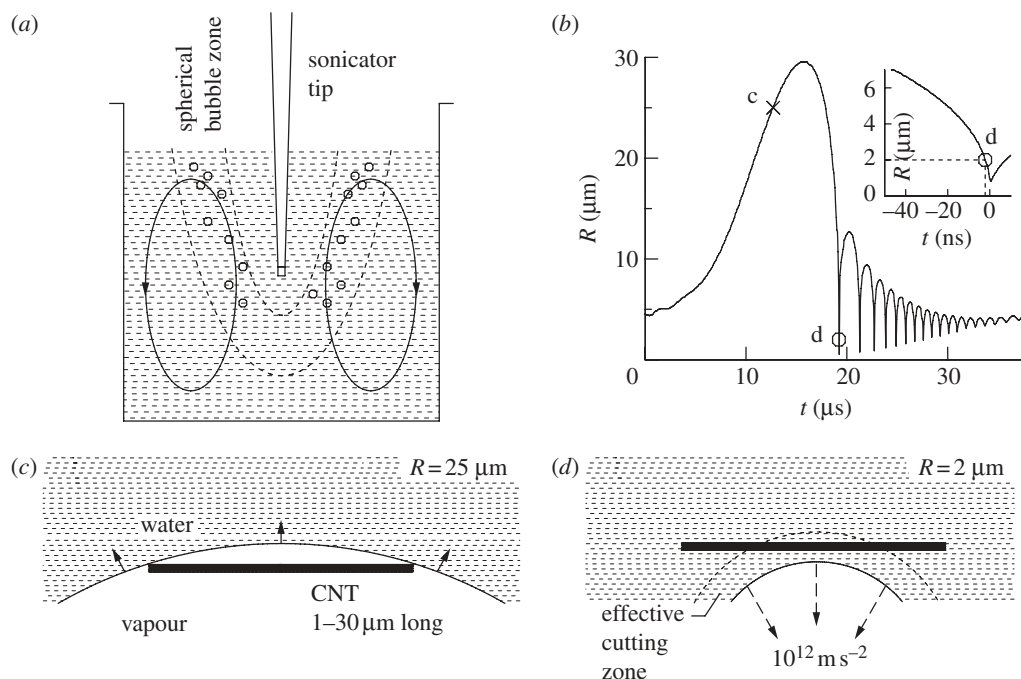
H. B. Chew et al.

Figure 1. Microbubble growth and collapse near a SWCNT during a sonication cycle. (*a*) Sonication of a SWCNT-dispersed aqueous medium by a sonicator creates a zone of spherical microbubbles where the nanotubes are effectively cut. (*b*) Rayleigh–Plesset solution of an evolving microbubble radius during a sonication cycle. (*c*) Hydrophobicity of the SWCNT wall makes the nanotube reside in the vapour side of the bubble during the bubble growth. (*d*) High acceleration of the bubble collapse causes the nanotube to submerge in the water side of the bubble.

in the vapour phase as shown in figure 1*c* owing to its hydrophobic repulsion. In contrast, at the final approximately 1 ns of the collapse, the bubble radius reduces to approximately 2 μm and the bubble wall experiences its maximum shrinking strain rate close to $10^9 \, \mathrm{s}^{-1}$, with sonoluminescence of approximately 200 ps duration occurring near the end (Brenner *et al.* 2002*a*). At this stage, the acceleration of bubble shrinkage approaches $10^{12} \, \mathrm{m \, s}^{-2}$, and the inertia force immerses the hydrophobic SWCNT into the water phase of the bubble, as shown in figure 1*d*. This excludes the possibility of high-temperature sonochemistry (Liu *et al.* 1998) since thermodynamic analysis shows that the temperature at the water-side of the bubble surface is basically the water temperature (Brenner *et al.* 2002*a*). Once a SWCNT lies parallel to the collapsing bubble wall, the rapidly shrinking water medium close to the bubble wall induces axial compressive forces on the nanotube, in contrast to previous speculations of tensile fracture (Hennrich *et al.* 2007). The size of this effective zone of compression in the axial direction of the nanotube is comparable to the approximately 2 μm diameter of the collapsing bubble at its maximum strain rate.

We have employed scale-bridging molecular dynamics (MD) simulations on massively parallel supercomputers to obtain a quantitative understanding of the nanotube cutting process within this zone of compression, and have validated these results with well-controlled sonication experiments.
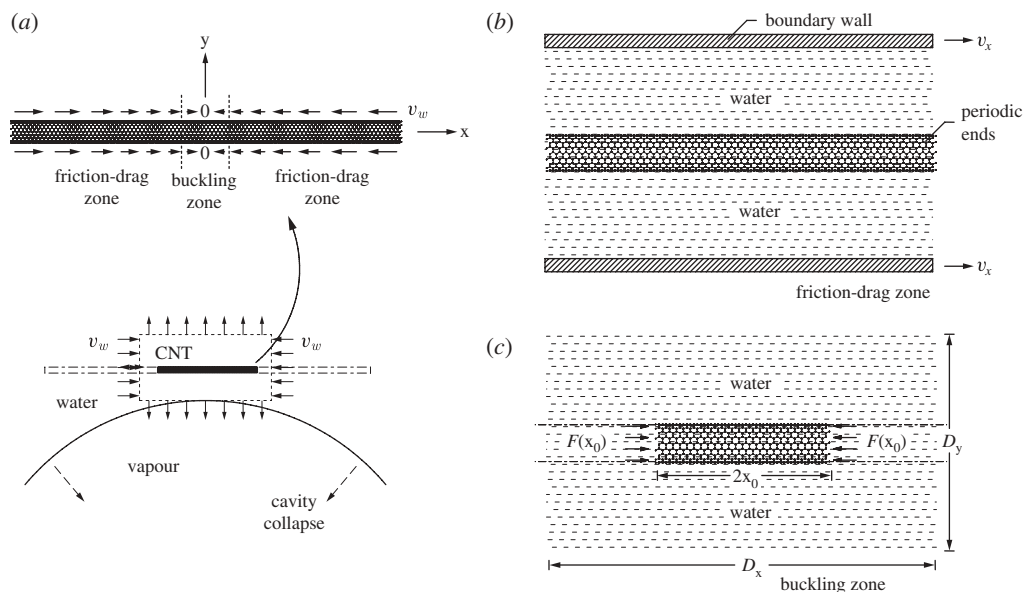
Figure 2. Scale-bridging procedure for modelling the SWCNT scission processes. (*a*) Flow-drag loading on a nanotube near the collapsing bubble. Arrows denote shrinking of water medium in the hoop direction and stretching in the normal direction to the bubble wall. Inset shows the domain of load transmission along the nanotube axis, which is subdivided into two zones; arrows denote the local relative flow velocity v_w along the nanotube. (*b*) Friction-drag calibration sub-domain, where axial motion of the domain boundaries drives the flow of water over the surface of a water-filled SWCNT. (*c*) Buckling simulation sub-domain, where the accumulated surface drag loads coupled with applicable end drag loads, is applied to the ends of a scale-reduced SWCNT in water.

2. Problem formulation for multi-scale modelling

For the quantitative modelling analysis, the free-body diagram of the effective compressive zone is shown in figure 2*a*. Since the direct modelling of this approximately 2 μm effective compressive zone cannot be handled as a single simulation unit in MD, we have devised a scale-bridging procedure in which the approximately 2 μm spatial domain of load transmission along the nanotube axis is sub-divided into sub-domains of friction drag and buckling processes. In the sub-domain of friction drag, we assume that the surface drag depends on the local relative flow velocity, $v_w = \dot{\varepsilon}x$, along the micron-length nanotube, and the velocity dependence is calibrated by MD simulations. Here, $\dot{\varepsilon}$ is the strain rate of the collapsing bubble wall and x the axial distance from the midpoint of the approximately 2 μm loading zone. For the friction-drag simulations, we employ an axially periodic water-filled simulation domain of $13 \times 8 \times 8\,\mathrm{nm}^3$ with a water-filled SWCNT sitting along the central axis of the domain (figure 2*b*). Owing to flow-slip conditions on the hydrophobic nanotube surfaces, the domain size is selected to be substantially larger than the nanotube diameter of approximately 1 nm but smaller than the minimum slip length (Majumder *et al.* 2005; Holt *et al.* 2006). The slip length varies from 10 to 500 nm for the velocity and defect density

range of our interest, as will be discussed in the following sections. The flow is
driven by the axial motion of the model-domain boundaries. The time-averaged
axial friction forces are then computed after achieving a steady-state flow within
50 ps. Using a similar simulation method, we next calibrate the induced drag at
the ends of the nanotube by fixing the one end and subjecting the other to water
flow. Finally, the effective loadings obtained from these calibrations are applied
at the ends of a scale-reduced 6 nm SWCNT in the middle of a $15 \times 5.5 \times 5.5 \, \text{nm}^3$
buckling simulation domain filled with water molecules (figure 2c).

   The nanotube–water systems described above are modelled using the classical
MD software LAMMPS (Plimpton 1995). The interaction between carbon atoms
is described by the AIREBO potential (Brenner *et al.* 2002b), while the water
intramolecular potential is modelled using TIP4P-Ew (Horn *et al.* 2004). The
carbon–water interactions are governed by a Lennard–Jones potential with the
equilibrium distance $\sigma_{\text{c-o}} = 0.319 \, \text{nm}$ and the potential depth $\varepsilon_{\text{c-o}} = 3.24 \, \text{meV}$.

3. Flow drag along single-walled carbon nanotube caused by bubble collapse

(*a*) *Two-state model of flow-slip on the single-walled carbon nanotube surface*

One of the most crucial steps of the cutting process simulation is the quantitative
analysis of the dynamic nano-fluidic flow over the SWCNT surface. During the
inflow of water over different diameter SWCNTs in figure 3a, our MD simulations
show distinct layering of water molecules surrounding the nanotubes. Closest to
each nanotube wall is a depletion zone where the density of water molecules is
very low. Next to this region, water molecules are tightly bunched together in a
closed ring in the projected cross-sectional view. This correlated layering of water
molecules leads to interfacial flow-slip as shown by the schematic in figure 3b. The
effective slip length is defined by

$$l_{\text{s}} = \frac{\mu[v]}{\tau}, \tag{3.1}$$

where τ is the flow-induced surface friction, μ the dynamic viscosity and $[v]$
the velocity jump across the nanotube–water interface. This flow-slip process
is distinctly different from the classical fluid mechanics assumption of a no-slip
boundary condition, which equates the fluid velocity at all fluid–solid boundaries
to that of the solid boundary. The correlated layering of water molecules can
also be seen in figure 3c, where the density of water molecules reaches a well-
defined peak, which, depending on the flow rate, can exceed twice the density
of water in the bulk. The peak is then trailed by decaying oscillatory bunching.
The corresponding streaming velocity profiles in figure 3d show a distinct velocity
jump at the water–nanotube interface for different bulk flow velocities.

   To model the flow-slip at the interface, we assume that the surface drag during
the flow of water over the hydrophobic SWCNT arises from a stick–slip type of
interaction between the water molecules and the carbon atoms. Although the
stick and slip states at the interface are partitioned in both time and space,
we homogenize the spatially partitioned stick and slip flow configurations as
a continuum flow and consider the temporal partitioning explicitly. For the
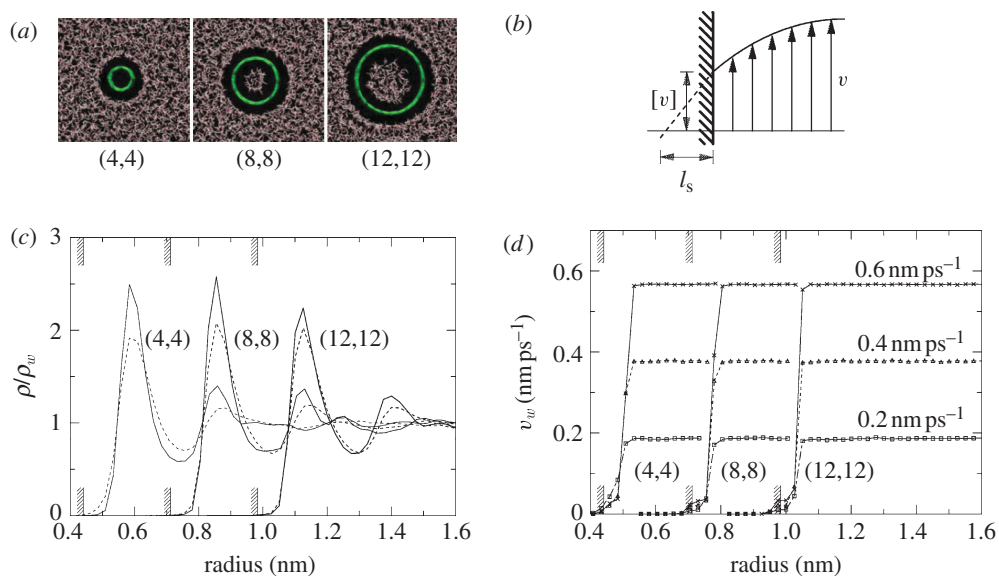water flowing over the surface with relative velocity V_0, we assume that the

Figure 3. Water–SWCNT interactions. (*a*) Cross-sectional view of the axial flow of water over (4,4), (8,8) and (12,12) SWCNTs with $v_w = 0.4 \, \text{nm ps}^{-1}$. (*b*) Schematic of flow-slip along an interface. (*c*) Normalized time-averaged radial density profile of the water medium surrounding the SWCNTs for two axial flow velocities. The bulk density of water is $\rho_w = 997 \, \text{kg m}^{-3}$. (*d*) Time-averaged axial velocity profile of water streaming over the SWCNTs depicting flow-slip process for three bulk flow velocities. The axis of the nanotubes in (*c*) and (*d*) is located at radius $= 0 \, \text{nm}$, while filled areas denote the wall boundaries of the different diameter nanotubes.

interface sticks for a duration of t^{st} periodically with the period of t_{p} for which $t^{\text{st}} \ll t_{\text{p}}$ as slip dominates during $t_{\text{p}} - t^{\text{st}}$. Furthermore, we introduce the stick interaction distance d^{st} over which a water molecule sticks to the carbon atom before it slips. The stick interaction distance is a material constant comparable to interatomic distance at the interface, with which the stick duration is expressed as $t^{\text{st}} = d^{\text{st}}/V_0 \leq t_{\text{p}}$. At low flow speeds, the stick interaction distance d^{st} is independent of V_0. However, at flow speeds comparable to the wave speed c of the interfacial slip at the water–nanotube interface, wave retardation effects become important and d^{st} is re-expressed as

$$d^{\text{st}} = \hat{d}_0 \sqrt{1 - (V_0/c)^2}, \tag{3.2}$$

where $\hat{d}_0$ denotes the quasi-static stick interaction distance at $V_0 = 0$.

The local friction at the water–nanotube interface, caused by the sudden sticking of water molecules moving with an average relative velocity V_0 to the nanotube, is given by

$$\tau^{\text{st}} = \rho \, V_0 \sqrt{\frac{\nu}{\pi t}}, \tag{3.3}$$

for $0 \leq t \leq t^{\text{st}}$, where ρ is the density and ν the kinematic viscosity of water (Rosenhead 1963). Then, the time-averaged surface drag over the stick–slip process, $(1/t_{\text{p}}) \int_0^{t^{\text{st}}} \tau^{\text{st}} \, dt$, is derived as

$$\bar{\tau}(V_0) = \frac{2\rho}{t_{\text{p}}} \sqrt{\frac{\nu \hat{d}_0 V_0 (1 - (V_0/c)^2)}{\pi}}. \tag{3.4}$$

Setting $[v] \approx V_0$ and $\tau = \bar{\tau}$ in equation (3.1), the corresponding slip length is then expressed as

$$l_{\text{s}} = l_0 \sqrt{\frac{V_0/c}{1 - (V_0/c)^2}}, \tag{3.5}$$

for which $l_0 = (t_{\text{p}}/2)\sqrt{\pi c \nu / \hat{d}_0}$. The frequency of interfacial interaction for the slip process, $1/t_{\text{p}}$, is typically in the range of 20–30 GHz which is close to the natural frequency of a hexagonal water molecule cluster in the bulk (Petrosyan 2005). The interface stick interaction distance $\hat{d}_0$, and hence l_0, depends heavily on the average intermolecular interaction strength across the solid–liquid interface, and also the defect state of the solid surface. Our MD calculations in the following section show that $\hat{d}_0$ is typically in the range of 0.03–2.3 nm for water flow over a SWCNT, and depends on the diameter and the defect density of the nanotube. For the overall response of the flow-slip, both the surface drag and the slip length depend on the wave speed of the interfacial slip c and the slip coefficient l_0, as shown in equations (3.4) and (3.5). These coefficients will be determined from our MD simulations.

(b) Load transmission from high-strain rate flow to single-walled carbon nanotube

The flow-slip process above is responsible for the ultralow friction at the water–nanotube interface as shown by our MD results for defect-free nanotubes in figure 4a,b, where effective slip lengths up to 450 nm are noted. Shown also are the two parameter (c and l_0) best fit of the slip lengths and traction distributions from MD with equations (3.4) and (3.5). The compressive axial forces arising from the accumulated traction distribution are concentrated in the middle of the nanotube as shown in figure 4c. For tube diameters smaller than (10,10), the surface-frictional stress decreases with increasing tube diameter owing to tube surface curvature effects (figure 4b). In this diameter range, the maximum axial force caused by the surface friction is nearly diameter indifferent (figure 4c), since the diameter-dependent friction area effect on the axial force is compensated by the effect of the curvature-dependent surface-friction stress. For nanotubes larger than (10,10) tube, the curvature effect on friction stress becomes negligible; in turn, the maximum axial load caused by surface friction becomes proportional to the nanotube diameter. When the nanotube is shorter than the approximately 2 μm effective loading zone size, the flow drag near the end of the nanotube (inset of figure 4c) is added to the surface drag and the maximum axial force increases with the diameter across the entire diameter range.
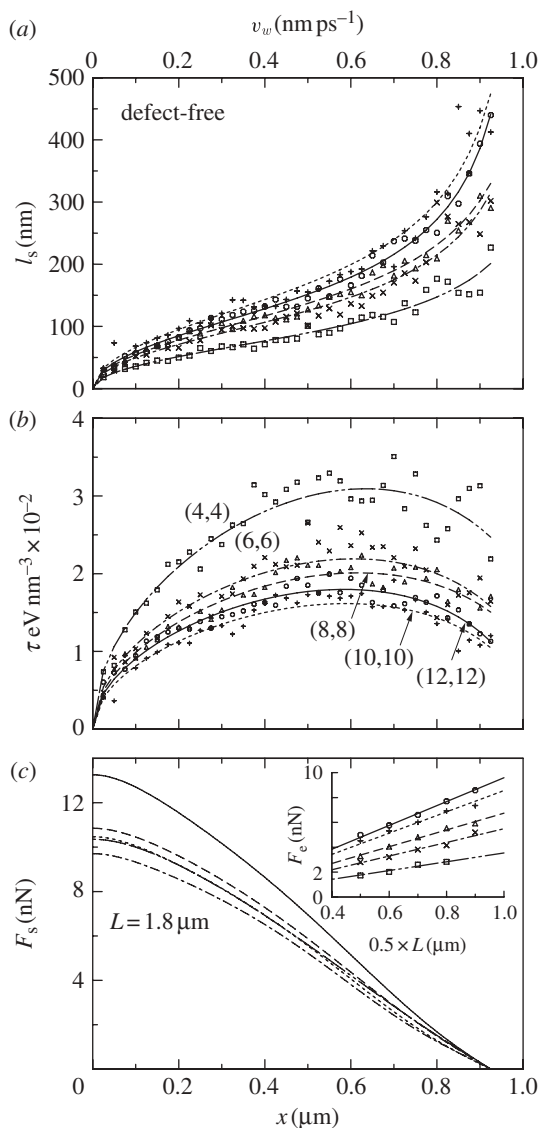
Figure 4. Flow-slip and drag along perfect armchair SWCNTs without defect. (*a*) Effective slip length l_s and (*b*) surface flow-drag distribution τ, for various local relative flow velocities v_w. The symbols denote the MD results, while the solid and dashed lines represent the two-parameter best fit to the analytical equations in (3.4) and (3.5). (*c*) Compressive axial loads F_s transmitted towards the middle of an $L = 1.8\,\mu\mathrm{m}$ length nanotube, caused by accumulated surface flow drag in (*b*). Inset in (*c*) shows effects of nanotube length and diameter on end drag loads F_e caused by inflow of water over the ends of the nanotube with velocity $v_w = \dot{\varepsilon}L/2$. (*a*) Squares with long dashed line, (4,4); crosses with dashed-dotted line, (6,6); triangles with short dashed line, (8,8); plus with dotted line, (10,10); circles with solid line, (12,12). (*c*) Long dashed line, (4,4); dashed-dotted line, (6,6); short dashed line, (8,8); dotted line, (10,10); solid line, (12,12).

Our MD simulations show that the large slip length, i.e. negligible friction, on the nanotube wall generates the maximum compressive axial loads in the range of 10–14 nN. These loads are far lower than the 60 nN required to buckle a pristine
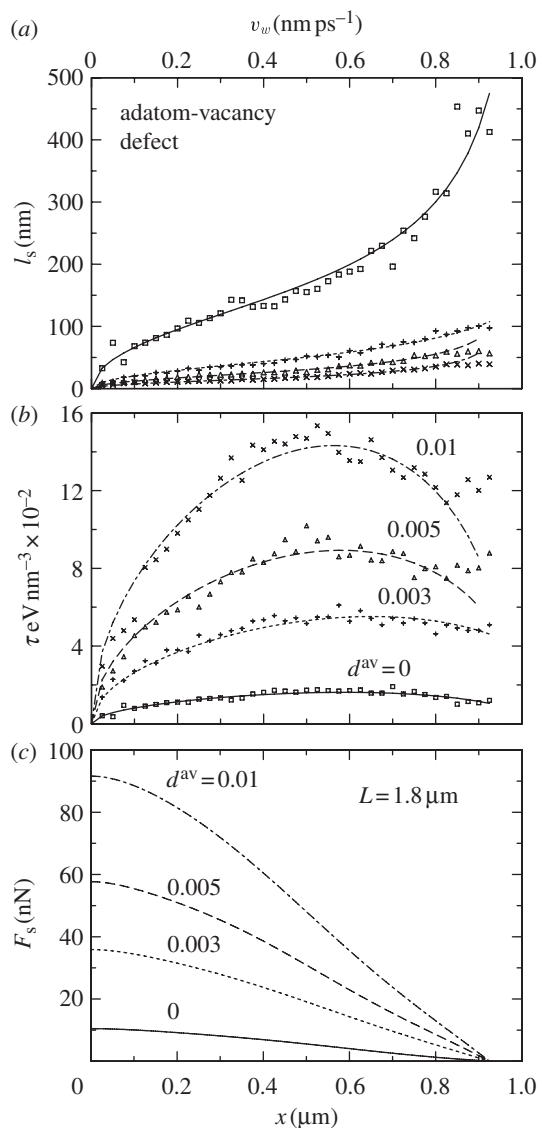
Figure 5. Flow-slip and drag along (10,10) SWCNTs with different adatom-vacancy defect densities d^{av}. (*a*) Effective slip length l_s and (*b*) surface flow-drag distribution τ, for various local relative flow velocities v_w. The symbols denote the MD results, while the solid and dashed lines represent the two-parameter best fit to the analytical equations in (3.4) and (3.5). (*c*) Compressive axial loads F_s transmitted towards the middle of an $L = 1.8\,\mu m$ length nanotube, caused by accumulated surface flow drag in (*b*). Squares with solid line, 0; plus with dotted line, 0.003; triangles with dashed line, 0.005; crosses with dashed-dotted line, 0.01.

SWCNT without defects. However, our simulations also show that the surface drag increases dramatically with the presence of a small percentage of adatom-vacancy defects (figure 5) or Stone-Wales defects (figure 6), and enhances the compressive loads in the middle of the tube. MD simulations of some adatom motions near the nanotube surface in this flow are shown in the electronic
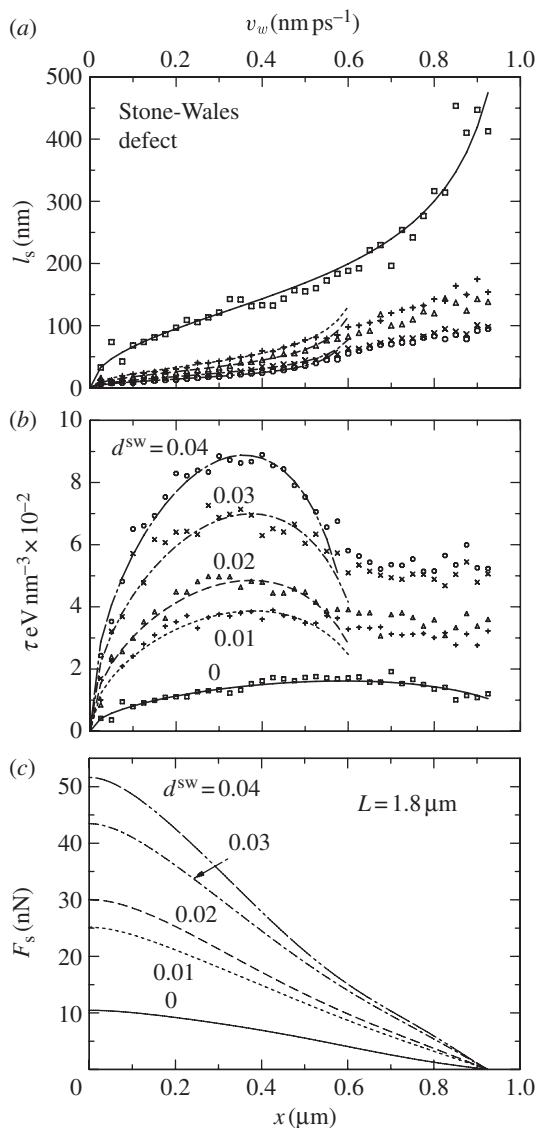
Figure 6. Flow-slip and drag along (10,10) SWCNTs with different Stone-Wales defect densities d^{SW}. (*a*) Effective slip length l_s and (*b*) surface flow-drag distribution τ, for various local relative flow velocities v_w. The symbols denote the MD results, while the solid and dashed lines represent the two-parameter best fit to the analytical equations in (3.4) and (3.5). (*c*) Compressive axial loads F_s transmitted towards the middle of an $L = 1.8\,\mu\text{m}$ length nanotube, caused by accumulated surface flow drag in (*b*). Squares with solid line, 0; plus with dotted line, 0.01; triangles with short dashed line, 0.02; crosses with dashed-dotted line, 0.03; circles with long dashed line, 0.04.

supplementary material, movie S1. Moved by the flow, adatoms often recombine to form larger molecular structures that obstruct the streamline inflow of water over the SWCNT. Stone-Wales defects, on the other hand, increase surface drag by distorting the curvature of the nanotube. While initial defects were created during the manufacturing of the nanotube, more defects are progressively

Table 1. Analytic parameters for wave speed of the interfacial slip c, slip coefficient l_0 and quasi-static stick interaction distance $\hat{d}_0$ determined from MD simulations.

	diameter effects on defect-free SWCNT			adatom-vacancy defects for (10,10) SWCNT				Stone-Wales defects for (10,10) SWCNT			
SWCNT	c (km s^{-1})	l_0 (nm)	$\hat{d}_0$ (nm)	d_{av}	c (km s^{-1})	l_0 (nm)	$\hat{d}_0$ (nm)	d_{SW}	c (km s^{-1})	l_0 (nm)	$\hat{d}_0$ (nm)
(4,4)	1.1	118	0.1	0	1.02	210	0.03	0	1.02	210	0.03
(6,6)	1.05	160	0.05	0.003	1.13	68	0.31	0.01	0.66	57	0.26
(8,8)	1.07	177	0.04	0.005	1	37	0.92	0.02	0.65	44	0.42
(10,10)	1.02	210	0.03	0.01	0.98	23	2.33	0.03	0.65	31	0.85
(12,12)	1.01	188	0.04					0.04	0.62	23	1.47

generated by the photons of sonoluminiscence during the sonication. The typical 6 eV photon energy of 200 nm wavelength light in the sonoluminiscence spectrum is believed to activate the formation of adatom-vacancy as well as Stone-Wales defects (Zhou & Shi 2003; Krasheninnikov *et al.* 2005).

The analytical expressions for surface drag and slip length in equations (3.4) and (3.5) are fitted with two fitting parameters c and l_0 to our MD results in figures 4–6 using the nonlinear least-square Marquardt–Levenberg algorithm (Marquardt 1963; Levenberg 1944). As shown by the solid and dashed lines in the figures, these analytical functions with just two fitting parameters well-describe both the flow-slip and surface friction profiles within the range of flow speeds of $0 \leq V_0 \leq c$, which validates our proposed stick–slip model analysis. Table 1 summarizes the fitted wave speeds of interfacial slip c, slip coefficient l_0 and the quasi-static stick interaction distance $\hat{d}_0$. For the evaluation of $\hat{d}_0$, we have assumed the interfacial interaction frequency of $1/t_p = 25$ GHz for the slip process (Petrosyan 2005). Observe that the wave speeds for defect-free nanotubes remain almost independent of the tube diameter at around 1.1 km s^{-1}. However, increasing tube diameter reduces the tube curvature and decreases the carbon–water interatomic interaction. This reduced interaction causes the decrease in $\hat{d}_0$ from 0.1 to 0.03 nm as the tube diameter increases from (4,4) to (10,10), with l_0 increasing from 118 to 210 nm as a consequence. For nanotubes larger than (10,10), both $\hat{d}_0$ and l_0 become almost diameter-indifferent and approach that for graphene. In the presence of defects, l_0 decreases substantially but the underlying mechanisms for the decrease are somewhat different for Stone-Wales defects and adatom-vacancy defects. For example, the presence of 1 per cent adatom-vacancy defects in a (10,10) nanotube increases $\hat{d}_0$ from 0.03 to 2.33 nm, but has no observable effect on c. In comparison, for a (10,10) tube with 1 per cent Stone-Wales defects, $\hat{d}_0$ increases from 0.03 to 0.26 nm, while c is dramatically lowered from 1.02 to 0.66 km s^{-1}. Therefore, the variation of l_0 for adatom-vacancy defects is mainly caused by the increase in $\hat{d}_0$, while that for Stone-Wales defects is mostly attributed to the drop in c.

4. Fracture of single-walled carbon nanotube by drag-induced axial compression

(*a*) *Dynamic shell bucking of SWCNT as a precursor of compressive fracture*

During microbubble collapse, inertia effects of the nanotube coupled with the short effective loading duration of the flow drag under 1 ns prevents the near micron-length nanotubes from collapsing in a long wavelength bending-beam buckling mode. Instead, the flow drag concentrates compressive axial forces in the middle of the effective compressive loading zone, at which the nanotube collapses readily in a localized axial shell-buckling mode to form alternate orthogonal folds (figure 7*a* and electronic supplementary material, movie S2). The critical shell-buckling load $f_c = 2\pi Eh^2/\sqrt{3(1-v^2)}$ as derived from continuum theory (Timoshenko & Gere 1961) is indifferent to the tube diameter, where E is the elastic modulus, v the Poisson's ratio and h the shell thickness of the tube. However, it is highly sensitive to the presence of defects in the tube. Figure 7*b,c* shows the critical shell-buckling load that depends on the density of adatom-vacancy and Stone–Wales defects in the tube. Plotted also in figure 7*b,c* are the maximum axial forces caused by flow drag on (10,10) nanotubes of different lengths, as functions of the defect density. When the density of the defects is high enough such that the drag-induced maximum axial force exceeds the critical buckling load, the nanotube buckles in the primary axial shell-buckling mode.

(*b*) *Compressive fracture by atom ejection*

It is well known that thin shell cylindrical structures like SWCNTs buckle under axial compression. However, it is still uncertain how buckling can cut SWCNTs, considering that folding ridges in a SWCNT caused by quasi-static Euler buckling make minimal damage and the deformation is highly reversible as observed in atomic force microscope (AFM) experiments (Falvo *et al.* 1997). Answering this question, our MD simulations reveal for the first time that the SWCNT has a peculiar compressive fracture mode of atom ejection. Under dynamic shell buckling, the stored elastic strain energy up to the onset of buckling is dynamically released and transformed to kinetic energy that is further focused into a more localized region during the post-buckling process. This final stage of energy focusing is so intense that a localized region in the tube becomes highly compressed such that atoms are spontaneously ejected out of the graphitic surface of the tube (figure 8*a* and electronic supplementary material, movie S3). The atom ejection cascades along a curved path on the graphitic surface with an average rate of one atom per 10 fs, which is equivalent to a 10–15 km s^{-1} crack propagation speed. This crack growth by atom ejection in a graphene sheet or a nanotube is only possible under dynamic compression. When the nanotube is compressed slowly, a beam-bending mode of buckling precedes to induce simple folding as shown in figure 8*b*. The simple folding process is nearly reversible, with the occasional breaking of one or two bonds but the bond breaking never cascades to cause crack growth.

The compressive fracture process by atomic ejection is unique to single atomic-sheet structures. Energy balance in cutting processes of an atomic sheet requires that the available energy per advancement of a crack, i.e. the energy release rate,
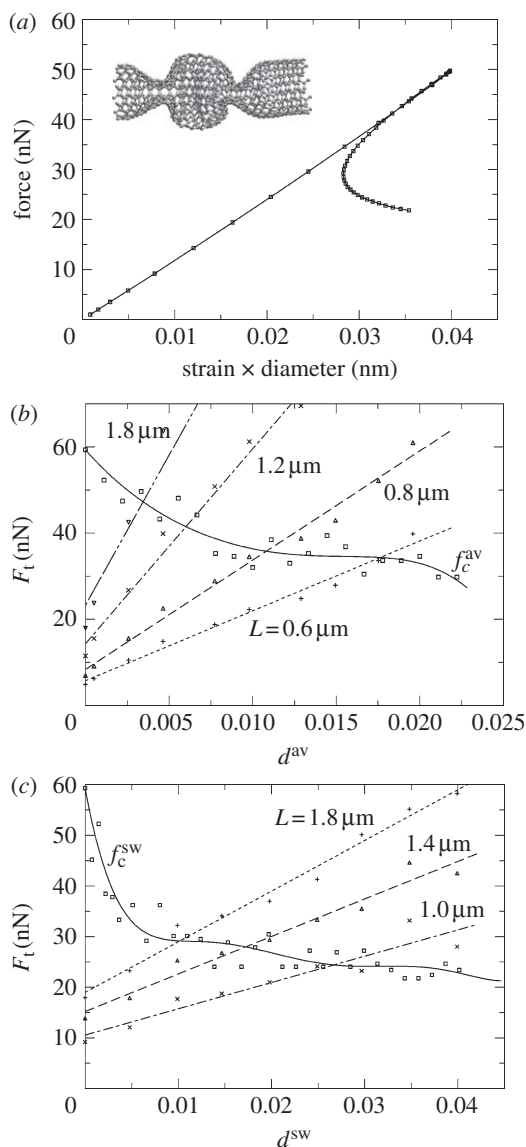
Figure 7. Shell buckling of (10,10) SWCNTs. (*a*) Finite element method analysis of the axial compressive load versus compressive strain up to the onset of shell buckling; inset shows the MD atomic configuration of the nanotube during symmetric shell buckling. (*b*) Critical dynamic shell-buckling loads f_c^{av} of the SWCNT in water for different adatom-vacancy defect densities d^{av}. (*c*) Critical dynamic shell-buckling loads f_c^{SW} of the SWCNT in water for different Stone-Wales defect densities d^{SW}. Dashed lines in (*b*) and (*c*) denote the maximum axial forces caused by flow drag on nanotubes of different lengths L as functions of the defect density, where both surface and end drags of the nanotube are considered.

must be sufficient to create the fracture surfaces (Griffith 1921). This energy release rate is proportional to the square of the stress intensity K around the crack-tip, i.e. $G = K^2/\bar{E}$ with $\bar{E}$ the effective elastic modulus of the atomic sheet, and thus is indifferent to the sign of the stress intensity (Irwin 1957;

Rice 1968). Therefore, both crack growth by crack-opening tension (figure 8*c*) and crack-closing compression (figure 8*d*), which create positive- and negative-stress intensities, respectively, are theoretically possible provided the mechanisms for crack growth are available. Up till now, however, crack growth under crack-closing compression has never been observed, even when the apparent far-field loading is compressive. Unlike conventional bond-breaking fracture under crack-opening tension, a mechanism is required to continuously remove atoms to prevent overlapping of the crack faces under crack-closing compression. For the first time, we have observed that such mechanism is possible in a single atomic sheet, and is operative in the cutting of SWCNTs. The energy release rate associated with this compressive fracture mode is found to be approximately $10 \, \mathrm{Jm}^{-2}$, with a corresponding stress intensity of approximately $-3 \, \mathrm{MPa}\sqrt{\mathrm{m}}$.

5. Experimental verification

The crack resulting from compressive atom ejection opens up almost half the circumference of the nanotube. However, the cut is often closed by bond reconstruction across the sites of the missing atoms, causing a local kink along the length of the nanotube. In search for evidence of these kinks, we have sonicated 1–$2 \, \mathrm{nm}$ diameter SWCNTs with lengths of 5–$30 \, \mu\mathrm{m}$ in distilled water. Relatively long SWCNTs were used to allow us to delineate the post-sonication characteristics of the nanotube. The SWCNTs, synthesized by catalytic chemical vapour deposition (CCVD) and later acid-purified, were obtained from Cheap Tubes Inc (Brattleboro, VT, USA). We dispersed $20 \, \mathrm{mg}$ of these nanotubes in $40 \, \mathrm{ml}$ of $100 \, \mathrm{mM}$ sodium cholate (Sigma Aldrich) D_2O solution using a $0.5''$ cup-horn sonicator (Branson digital sonifer D450, $400 \, \mathrm{W}$ maximum power, $20 \, \mathrm{kHz}$) at $40 \, \mathrm{W}$ power for $1 \, \mathrm{h}$ while cooling the solution in an ice bath. The resulting suspension was then subjected to centrifugation at $10 \, 000 \, g$ for $30 \, \mathrm{min}$ (Eppendorf 5810 R, 5000 r.p.m.) to remove larger agglomerates prior to sonication. Thereafter, $1 \, \mathrm{ml}$ of this solution was diluted by a factor of 10 with $1 \, \mathrm{wt\%}$ sodium cholate D_2O solution in a $10 \, \mathrm{ml}$ Pyrex beaker and subjected to high-power sonication at $80 \, \mathrm{W}$ power with a micro-tip probe, while continuously cooled in an ice bath. Our experiments show that there is an optimal sonication power window of 60–$80 \, \mathrm{W}$ for effective cutting of the SWCNTs. At higher sonication power, the cavitated microbubbles become non-spherical during their collapse, and the nanotube cutting efficiency is substantially reduced. Samples for electrophoresis and AFM imaging were taken after 1, 3, 5, 8 and $12 \, \mathrm{h}$, while scanning tunnelling microscopy (STM) and high-resolution transmission electron microscopy (HR-TEM) were used to image the kinked SWCNTs after $12 \, \mathrm{h}$ of sonication.

Gel electrophoresis on the respective samples was performed in a $7 \times 13 \, \mathrm{cm}$, $1 \, \mathrm{wt\%}$ agarose gel in a $40 \, \mathrm{mM}$ Tris acetate-EDTA buffer (Sigma-Aldrich) with $25 \, \mathrm{mM}$ sodium cholate D_2O solution at $150 \, \mathrm{V}$ (field strength of $7 \, \mathrm{V \, cm}^{-1}$) for $30 \, \mathrm{min}$. Separately, AFM samples for imaging were obtained by depositing the surfactant-stabilized nanotubes onto the freshly cleaved surface of highly oriented pyrolytic graphite (HOPG). AFM images were taken in the tapping mode using a Digital Instruments Dimensions 3100 SPM with NSC15/AIBS silicon probes (MikroMasch). We performed STM imaging on the post-sonicated nanotubes deposited on the HOPG substrate using a Nanoscope III scanning
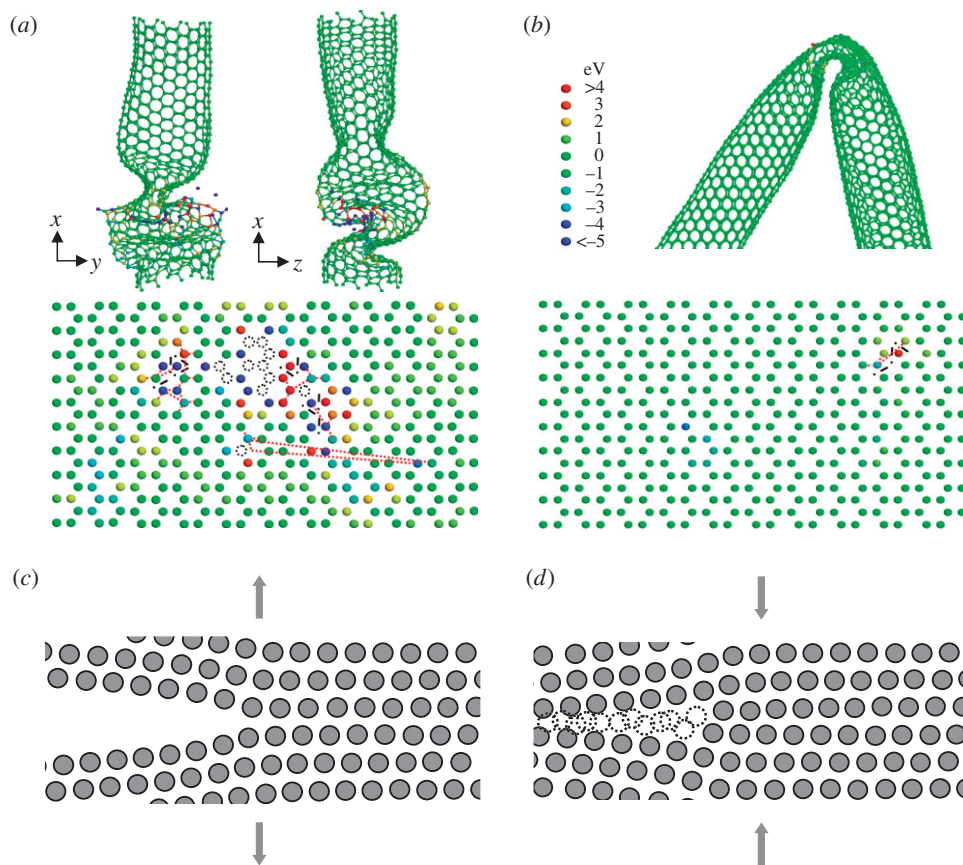
Figure 8. Compressive atom ejection. (*a*) Cascade atom ejection during post-buckling (top); locations of ejected atoms in the initial undeformed atomic configuration of the unwrapped SWCNT wall (bottom). (*b*) Beam-bending buckling of the nanotube under quasi-static loading. Atomic energy levels denote the average atomic bond energies with positive and negative signs indicating average bond stretching or compression. (*c,d*) Schematic of crack growth under crack-opening tension and crack-closing compression, respectively. (*a,b*) Red dotted lines, sp3 bond; dashed-dotted lines, bond break; dotted circles, atom ejection.

tunnelling microscope (Digital Instruments) operating in constant current mode under ambient conditions at 18°C; the STM tip was prepared by cutting a 0.25 mm diameter platinum/rhodium (87/13) wire (Omega). HR-TEM (Tecnai, FEI company) operating at 200 kV was used to image the 12 h post-sonicated nanotubes deposited on a copper grid with 10–20 nm carbon thin film. In all cases, the images were taken without post-sonication treatments such as acetone dilution, centrifugal separation of surfactants or electrophoresis, to avoid post-sonication damage.

(*a*) Post-sonication observation of partially cut single-walled carbon nanotubes

The spreads of the sonicated SWCNTs in agarose gel electrophoresis are shown in figure 9*a*. The longer the nanotubes were sonicated, the more they spread in the gel, indicating that sonication progressively cuts the nanotube. However, the spreadings of SWCNTs exhibit gradual density variations resembling candle
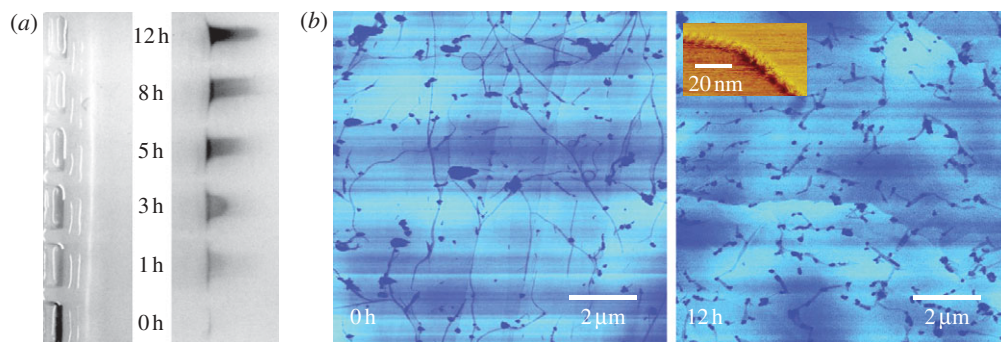
Figure 9. Ultrasonication experiments of SWCNTs in water. (*a*) Spreadings of SWCNTs in agarose gel electrophoresis: the nanotubes were dispersed by sodium cholate surfactant and sonicated in distilled water for 0, 1, 3, 5, 8 and 12 h. (*b*) AFM images of the nanotubes on an HOPG surface before sonication and after 12 h sonication; inset in the right frame shows a STM image of a SWCNT kink on an HOPG surface after 12 h sonication.

flames. Figure 9*b* shows AFM/STM images of SWCNTs before and after sonication. The sonicated nanotubes show approximately 0.25 μm (or shorter) lengths of kinked nanotube fragments linked together. The fragment size distribution after 12 h of sonication suggests that an average of approximately 10 cuts per sonication cycle were made. Closer examination reveals that the total length for some of these linked segments remains close to the approximately 18 μm average initial length of the nanotubes before sonication. These interconnected kinked fragments entail that SWCNTs sonicated in water are mostly cut partially and in compression; in contrast, such kinks are seldom observed in AFM images of SWCNTs sonicated in acid (Liu *et al.* 1998), since the remaining ligaments of the partial cuts are attacked by acid to be fully severed. The candle-flame-like electrophoresis spreadings of these partially cut SWCNTs are distinctly different from those for fully cut SWCNTs (Heller *et al.* 2004). While uncorrelated spreading of the fully cut nanotubes results in uniform density distributions, the correlated spreading of partially cut SWCNTs of 5–30 μm initial length induces the gradual density variations shown in figure 9*a*. These experiments confirm our MD results that the SWCNTs are partially cut during ultrasonication processes in water.

(*b*) *Assessment of kink angles caused by dynamic atom ejection*

When a nanotube with multiple kinks is placed on an HOPG substrate, the straight portions of the nanotube are aligned with the crystallographic orientations of minimum energy configuration for adhesion on the surface. The alignment makes large-angle zigzag shape configurations, as shown in the second frame of figure 9*b*. When the nanotube is placed on an amorphous carbon film under HR-TEM observation, the multiple kinks create a layout configuration comprised of distinct straight and bent segments along random orientations, as shown in figure 10*a*. The bent angle of the nanotube is primarily determined by the end attachment conditions of the nanotube. To ascertain the pre-loaded kink angle of a freely suspended nanotube, we perform finite-element analysis of possible bent configurations of the segment PQ in figure 10*a*. To this end, a (10,10) SWCNT with a pre-loaded kink is modelled using four-noded
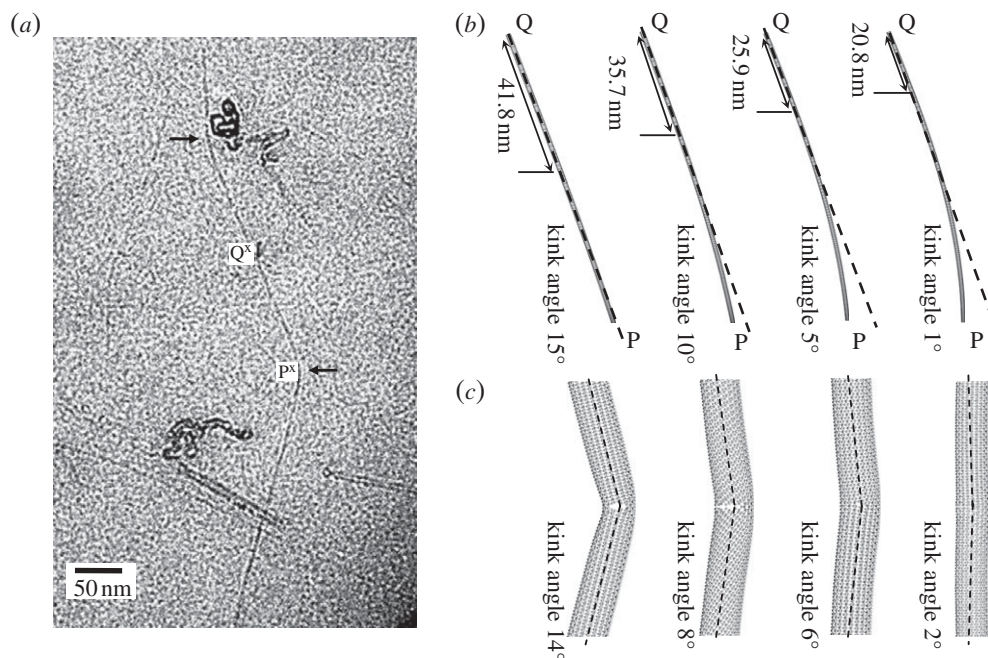
Figure 10. Kink angle assessment. (*a*) HR-TEM image of distinctive straight and bent segments of the nanotube deposited on amorphous carbon film after 12 h of sonication. Arrows denote the kink locations along the nanotube. (*b*) FEM analysis of possible bent configurations of the segment PQ in (*a*) with different pre-loaded kink angles. (*c*) Molecular statics simulations of the pre-loaded kink angles formed by the removal of 1 to 4 (right to left) rows of atoms across the half-section of the tube.

quadrilateral shell elements with equivalent continuum shell properties of the nanotube (Yakobson *et al.* 1996). Roller boundary conditions are enforced at the kinked end P, while the middle of the straight tube section at Q is subjected to incremental vertical displacement loading until the angle subtended by the straight-end segment reaches the experimental bend angle of 18.5° (figure 10*b*). Separately, molecular statics simulations are used to ascertain the possible pre-loaded kink angles made by cut closure across a different number of rows of missing half-section of atoms from a pristine SWCNT at P (figure 10*c*). Comparisons between the bent configuration of the nanotube observed in figure 10*a* and those of figure 10*b*,*c* suggest that the zone of atomic ejection across the half-section of the tube is approximately two to three rows of atoms, which is consistent with the MD simulation results.

6. Discussions and conclusions

As discussed above, fracture by compressive atom ejection is the critical precursor mechanism of cutting SWCNTs with ultrasonication. The cutting rate during sonication is governed by the competition between load increase and structural degradation caused by progressive generation of sonoluminescence-induced defects. In the successive cutting process during sonication, much of
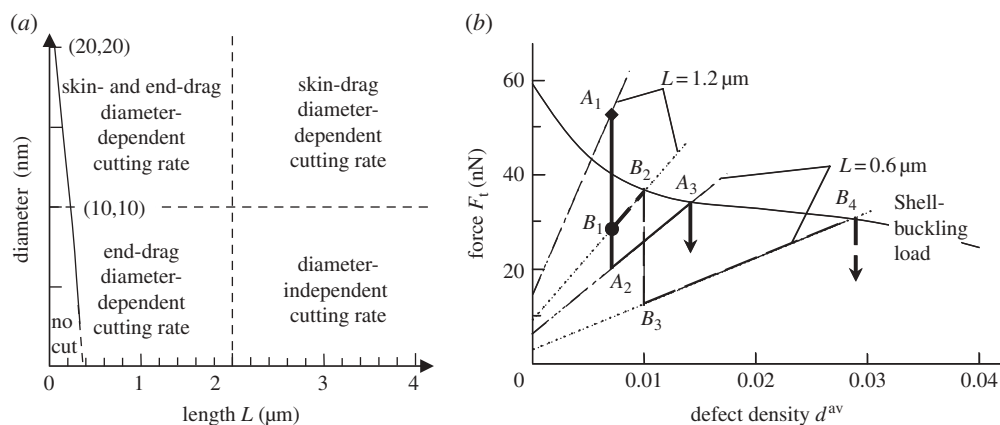
Figure 11. (*a*) Map of diameter and length-dependent SWCNT cutting rate for fixed initial density of defects. (*b*) Different cutting processes (bold dashed and solid lines) of (6,6) and (12,12) nanotubes with the same initial adatom-vacancy defect density. (*b*) Dotted lines, (6,6); dashed-dotted lines, (12,12).

the time is spent on creating defects which will increase the drag and reduce the critical shell-buckling load to trigger the cutting. The drag-induced axial load depends on the diameter, length and defect density, while the critical shell-buckling load is only dependent on defect density. The effects of all these parameters on the cutting rate are summarized in figure 11.

The map in figure 11*a* shows that the terminal length of the SWCNTs cut by prolonged ultrasonication in water is approximately 50–200 nm depending on the diameter of the nanotube. However, it can still be further shortened by chemical reactions in strong acids. The map also shows that the cutting rate is diameter-dependent for SWCNTs shorter than approximately 2 μm predominantly owing to the flow drag near the end of the tube, with larger diameter nanotubes being cut faster. When the nanotube is longer than approximately 2 μm, the cutting rate depends on the diameter if the diameter is larger than that of a (10,10) tube, but it is diameter independent for nanotubes of smaller diameter. As an example, the cutting processes of (6,6) and (12,12) nanotubes of 1.2 μm length with the same initial adatom-vacancy defect density of 0.7 per cent are compared in figure 11*b*. At the beginning of ultrasonication, the maximum axial force in the (12,12) nanotube, depicted as A_1, is already greater than the critical buckling load and the nanotube buckles to be cut in half to the point A_2. On the other hand, the maximum axial force in the (6,6) nanotube, depicted as B_1, is below the critical buckling load. Ultrasonication should be carried out to create defects until the defect density reaches B_2 where the maximum axial force is increased to the level of the critical buckling load; then, the (6,6) nanotube is cut in half to point B_3. For further cutting, the (6,6) nanotube must be sonicated even longer from B_3 to B_4 than the (12,12) tube from A_2 to A_3. However, the difference between the initial defect densities in the different diameter nanotubes can reverse the apparent dependence of the cutting rate on the diameter (Heller *et al.* 2004; Casey *et al.* 2008).

In conclusion, we have shown in detail, with large-scale supercomputing simulations and experiments that multi-scale energy-focusing mechanisms are hierarchically operative in cutting the SWCNTs under ultrasonication. These

mechanisms include microbubble collapse, defect generation in the nanotubes by sonoluminescence, nanotube axial compression caused by nanoscale flow drag, dynamic shell buckling of the nanotubes and compressive atom ejection in post-shell-buckling processes. In particular, fracture by compressive atom ejection is found to be the critical precursor mechanism of cutting SWCNTs with sonication. If sonicated in water, this cutting mechanism ultimately leads to the formation of multiple kinks along the nanotube, which are highly attractive intramolecular junctions (Yao *et al.* 1999; Ouyang *et al.* 2001) for building molecular-scale electronics. Knowing the fundamental cutting mechanism provides insights to develop new manufacturing and sorting processes of SWCNTs with different diameters, lengths and chiralities. More importantly, we have discovered that cracks can dynamically grow with atom ejection under crack-closing compression in graphene-like nanostructures. This mechanism is fundamentally different from previously reported phenomena such as the scission of a primary bond in a polymer chain (Kuijpers *et al.* 2004) or tensile failure of a SWCNT induced by plastic elongation (Bosovic *et al.* 2003). This unique atomic-sheet fracture mechanism can explain the formation of holes in sonicated graphene sheets (Si & Samulski 2008), and is expected to play an important role in furthering our understanding of other compressive atomic-scale events such as ion beam bombardment, laser ablation, shock wave loading and focused ion beam milling of graphene-like structures.

References

Bosovic, D., Bockrath, M., Hafner, J. H., Lieber, C. M., Park, H. & Tinkham, M. 2003 Plastic deformations in mechanically strained single-walled carbon nanotubes. *Phys. Rev. B* **67**, 033407. (doi:10.1103/PhysRevB.67.033407)

Brenner, M. P., Hilgenfeldt, S. & Lohse, D. 2002*a* Single-bubble sonoluminescence. *Rev. Mod. Phys.* **74**, 425–484. (doi:10.1103/RevModPhys.74.425)

Brenner, D. W., Shenderova, O. A., Harrison, J. A., Stuart, S. J., Ni, B. & Sinnott, S. B. 2002*b* A second-generation reactive empirical bond order (REBO) potential energy expression for hydrocarbons. *J. Phys. Condens. Matter* **14**, 783–802. (doi:10.1088/0953-8984/14/4/312)

Casey, J. P., Bachilo, S. M., Moran, C. H. & Weisman, R. B. 2008 Chirality-resolved length analysis of single-walled carbon nanotube samples through shear-aligned photoluminescence anisotropy. *ACS Nano* **2**, 1738–1746. (doi:10.1021/nn800351n)

Falvo, M. R., Clary, G. J., Taylor II, R. M., Chi, V., Brooks Jr, F. P., Washburn, S. & Superfine, R. 1997 Bending and buckling of carbon nanotubes under large strain. *Nature* **389**, 582–584. (doi:10.1038/39282)

Flannigan, D. J. & Suslick, K. S. 2005 Plasma formation and temperature measurement during single-bubble cavitation. *Nature* **434**, 52–55. (doi:10.1038/nature03361)

Griffith, A. A. 1921 The phenomena of rupture and flow in solids. *Phil. Trans. R. Soc. Lond. A* **221**, 163–198. (doi:10.1098/rsta.1921.0006)

Hennrich, F., Krupke, R., Arnold, K., Stütz, J. A. R., Lebedkin, S., Koch, T., Schimmel, T. & Kappes, M. M. 2007 The mechanism of cavitation-induced scission of single-walled carbon nanotubes. *J. Phys. Chem. B* **111**, 1932–1937. (doi:10.1021/jp065262n)

Heller, D. A., Mayrhofer, R. M., Baik, S., Grinkova, Y. V., Usrey, M. L. & Strano, M. S. 2004 Concomitant length and diameter separation of single-walled carbon nanotubes. *J. Am. Chem. Soc.* **126**, 14567–14573. (doi:10.1021/ja046450z)

Holt, J. K., Park, H. G., Wang, Y., Stadermann, M., Artyukhin, A. B., Grigoropoulos, C. P., Noy, A. & Bakajin, O. 2006 Fast mass transport through sub-2-nanometer carbon nanotubes. *Science* **312**, 1034–1037. (doi:10.1126/science.1126298)

Horn, H. W., Swope, W. C. & Pitera, J. W. 2004 Development of an improved four-site water model for biomolecular simulations: TIP4P-Ew. *J. Chem. Phys.* **120**, 9665–9678. (doi:10.1063/1.1683075)

Irwin, G. 1957 Analysis of stresses and strains near the end of a crack traversing a plate. *J. Appl. Mech.* **24**, 361–364.

Iijima, S. 1991 Helical microtubules of graphitic carbon. *Nature* **354**, 56–58. (doi:10.1038/354056a0)

Krasheninnikov, A. V., Banhart, F., Li, J. X., Foster, A. S. & Nieminen, R. M. 2005 Stability of carbon nanotubes under electron irradiation: role of tube diameter and chirality. *Phys. Rev. B* **72**, 125428. (doi:10.1103/PhysRevB.72.125428)

Kuijpers, M. W. A., Iedema, P. D., Kemmere, M. F. & Keurentjes, J. T. F. 2004 The mechanism of cavitation-induced polymer scission; experimental and computational verification. *Polymer* **45**, 6461–6467. (doi:10.1016/j.polymer.2004.06.051)

Liu, J. *et al.* 1998 Fullerene pipes. *Science* **280**, 1253–1256. (doi:10.1126/science.280.5367.1253)

Levenberg, K. 1944 A method for the solution of certain problems in least squares. *Quart. Appl. Math.* **2**, 164–168.

Majumder, M., Chopra, N., Andrews, R. & Hinds, B. J. 2005 Nanoscale hydrodynamics: enhanced flow in carbon nanotubes. *Nature* **438**, 44. (doi:10.1038/43844a)

Marquardt, D. 1963 An algorithm for least-squares estimation of nonlinear parameters. *SIAM J. Appl. Math.* **11**, 431–441. (doi:10.1137/0111030)

Matula, T. J. 1999 Inertial cavitation and single-bubble sonoluminescence. *Phil. Trans. R. Soc. Lond. A* **357**, 225–249. (doi:10.1098/rsta.1999.0325)

McNamara III, W. B., Didenko, Y. T. & Suslick, K. S. 1999 Sonoluminescence temperatures during multi-bubble cavitation. *Nature* **401**, 772–775. (doi:10.1038/43872)

Ouyang, M., Huang, J.-L., Cheung, C. L. & Lieber, C. M. 2001 Atomically resolved single-walled carbon nanotube intramolecular junctions. *Science* **291**, 97–100. (doi:10.1126/science.291.5501.97)

Petrosyan, V. I. 2005 Resonance RF emission from water. *Tech. Phys. Lett.* **31**, 1007–1008. (doi:10.1134/1.2150882)

Plimpton, S. J. 1995 Fast parallel algorithms for short-range molecular dynamics. *J. Comp. Phys.* **117**, 1–19. (doi:10.1006/jcph.1995.1039)

Plesset, M. S. & Prosperetti, A. 1977 Bubble dynamics and cavitation. *Annu. Rev. Fluid Mech.* **9**, 145–185. (doi:10.1146/annurev.fl.09.010177.001045)

Rayleigh, L. 1917 On the pressure developed in a liquid during the collapse of a spherical cavity. *Philos. Mag.* **34**, 94–98.

Rice, J. R. 1968 A path independent integral and the approximate analysis of strain concentration by notches and cracks. *J. Appl. Mech.* **35**, 379–386.

Rosenhead, L. 1963 *Laminar boundary layers: fluid motion memoirs.* Oxford, UK: Oxford University Press.

Si, Y. & Samulski, E. T. 2008 Synthesis of water soluble graphene. *Nano Lett.* **8**, 1679–1682. (doi:10.1021/nl080604h)

Suslick, K. S. & Flannigan, D. J. 2008 Inside a collapsing bubble: sonoluminescence and the conditions during cavitation. *Annu. Rev. Phys. Chem.* **59**, 659–683. (doi:10.1146/annurev.physchem.59.032607.093739)

Timoshenko, S. P. & Gere, J. M. 1961 *Theory of elastic stability.* New York, NY: McGraw-Hill.

Yakobson, B. I., Brabec, C. J. & Bernholc, J. 1996 Nanomechanics of carbon tubes: instabilities beyond linear response. *Phys. Rev. Lett.* **76**, 2511. (doi:10.1103/PhysRevLett.76.2511)

Yao, Z., Postma, H. W. Ch., Balents, L. & Dekker, C. 1999 Carbon nanotube intramolecular junctions. *Nature* **402**, 273–276. (doi:10.1038/46241)

Zhou, L. G. & Shi, S.-Q. 2003 Formation energy of Stone-Wales defects in carbon nanotubes. *Appl. Phys. Lett.* **83**, 1222–1224. (doi:10.1063/1.1599961)